

The Dispersion Characteristics of the Three-Dimensional Function Photonic Crystals with Woodpile Lattices Composed of Plasma and Magnetized Plasma Elements

Hai-Feng Zhang^{1-5, *} and Hao Zhang¹

Abstract—The dispersion characteristics of woodpile three-dimensional (3D) function photonic crystals (PCs) composed of the plasma and function dielectric elements are theoretically investigated by a modified plane wave expansion method, respectively, and the formulas to obtain the dispersion diagrams are given. Only two cases are considered, which are the presence and absence of the external magnetic field. The external magnetic field is vertical to the wave vector, which means that only the magneto-optical Voigt effect is considered. For the proposed PCs, the function dielectric square columns are inserted into the plasma background with face-centered-tetragonal symmetry according to the woodpile lattices. The relationships between the parameters of such PCs and the features of the photonic band gaps (PBGs) for the extraordinary mode and electromagnetic wave are studied under two different cases. The calculated results show that the dispersion characteristics of the proposed PCs can be tailored by adjusting those parameters. If the extrinsic magnetic field does not exist, larger PBG can be found in the present PCs than 3D dielectric-air PCs, 3D function dielectric PCs and 3D plasma-dielectric PCs with the same lattices. If there is an external magnetic field, a narrower PBG for the extraordinary mode can be obtained than the 3D function dielectric PCs and 3D plasma-dielectric PCs with the same lattices. The computed results also show us an approach to realize the reconfigurable devices based on the PCs.

1. INTRODUCTION

In 1987, photonic crystals (PCs) as a novel idea were firstly reported [1,2], which have been fully investigated both theoretically and experimentally in the past few decades. Based on the definition of PCs, PCs are different kinds of materials arrayed periodically in the space. It means that PCs include one-dimensional (1D), two-dimensional (2D) and three-dimensional (3D) cases. One of the interesting features of PCs is the ability to produce photonic band gaps (PBGs) [3]. In the frequency regions of PBGs, the incident light is forbidden to propagate through the PCs. Numerous amazing devices can be realized by PCs. In 2004, Hojo and co-workers [4] proposed a new concept called plasma photonic crystals (PPCs). The interesting characteristic of PPCs is producing “*tunable*” PBGs. Since then, PPCs have become a novel research hotspot. Unlike ordinary dielectric PCs, the physical features for plasma can be adjusted obviously by a lot of external factors [5], such as extrinsic magnetic field,

Received 3 September 2018, Accepted 5 November 2018, Scheduled 19 November 2018

* Corresponding author: Hai-Feng Zhang (hanlor@163.com).

¹ College of Electronic and Optical Engineering & College of Microelectronics, Nanjing University of Posts and Telecommunications, Nanjing 210023, China. ² National Electronic Science and Technology Experimental Teaching Demonstrating Center, Nanjing University of Posts and Telecommunications, Nanjing 210023, China. ³ National Information and Electronic Technology Virtual Simulation Experiment Teaching Center, Nanjing University of Posts and Telecommunications, Nanjing 210023, China. ⁴ Key Laboratory of Radar Imaging and Microwave Photonics (Nanjing Univ. Aeronaut. Astronaut.), Ministry of Education, Nanjing University of Aeronautics and Astronautics, Nanjing 210016, China. ⁵ State Key Laboratory of Millimeter Waves of Southeast University, Nanjing 210096, China.

extrinsic voltage, and gas pressure. Obviously, realizing reconfigurable applications by PPCs is a good choice [6–8]. Unlike the conventional PCs with different dielectric constituents, not only the PPCs have interesting dispersion properties [9–11], but also some useful properties can be obtained, such as broadened PBG [12], magnetically changed PBG [13] and tailored defect modes [14]. On the other hand, PPCs also belong to a kind of metamaterials [15] under some specific conditions. Consequently, PPCs can present some abnormal properties, such as complex magneto-optical effects [16], properties of nonreciprocal propagation [17] and nonlinear features [18]. Therefore, 3D PPCs and the novel applications of PPCs became new research fields. Especially, if an extrinsic magnetic field is introduced into PPCs, magnetized plasma photonic crystals (MPPCs) [19–21] can be realized. If the directions of extrinsic magnetic field and wave vector remain vertical, magneto-optical Voigt effect can be seen in MPPCs. Qi hang [22] and Zhang et al. [23] also used the periodical arrangement of extrinsic magnetic field to plasma block to realize 1D and 2D MPPCs, when Voigt effect is considered. They found that PBGs can be manipulated by extrinsic magnetic field. Compared with PPCs, more interesting properties and more complicated EM modes can be found in MPPCs.

3D PCs are more preferred to realize complete PBGs than 1D and 2D cases. In the last few years, the characteristics of 3D PPCs and MPPCs were systematically reported by Zhang and co-workers [24–26], and they demonstrated that adjustable PBGs and flatbands region (FBR) can be seen. However, only some simple theoretical models are considered in their reports. For instance, the embedded fillers for PPCs are spheres, and the dielectric spheres are inserted into the plasma background (or complementary structure) with simple-cubic, diamond and face-centered-cubic lattices, respectively. Obviously, those models can hardly be fabricated in reality, and the regions of obtained PBGs are relatively narrow. In order to widen the PBG of PCs, Ho et al. [27] present woodpile lattices to broaden the PBGs. Similar reports can also be seen in [28, 29]. Compared with those conventional lattices as described in the reports of Zhang et al. [24–26], the PCs with woodpile lattices can produce larger PBGs. As mentioned above, the PCs with woodpile lattices are more feasible to realize the practical devices. In addition to changing the lattices of PCs, there are also some other ways to widen the PBGs [30, 31]. PCs with “*dispersion*” or “*nonlinear*” dielectrics as an element is another method [18]. The “*nonlinear*” dielectrics belong to the “*function*” dielectrics. For instance, the Kerr nonlinear dielectric is a kind of such “*function*” dielectrics. It means that its permittivity can be written as a function of the space ordinates \mathbf{r} . The interesting properties can be achieved in PCs with such “*function*” dielectrics [32–34]. Recently, the features of “*function*” photonic crystals have also been reported by some researchers [35–37]. Obviously, Their research results illustrated that adjustable PBGs can be achieved when the parameters of “*function*” dielectrics are changed. Until now, the dispersion features of 3D woodpile function PCs composed of plasma (FPPCs) and magnetized plasma elements (FMPPCs) have hardly been investigated. Of course, in addition to FPPCs and FMPPCs, metallodielectric PCs and plasmonic PCs are also very important areas of research in recent years [38–44].

As described above, the purpose of this manuscript is to investigate the dispersion features of woodpile 3D FPPCs and FMPPCs in theory. For the proposed FPPCs and FMPPCs, function dielectric square columns are inserted into the plasma background with face-centered-tetragonal symmetry according to the woodpile lattices. The dispersion curves of those woodpile FPPCs and FMPPCs are calculated by the plane wave expansion (PWE) method. The relative permittivity of function dielectric square columns can be expressed as a function of the space coordinates and function coefficient. In the following sections, we consider that angular frequency is ω .

2. THEORETICAL MODEL AND FORMULAS

In Fig. 1, spatial structure diagrams of the proposed 3D FPPCs and FMPPCs, the first irreducible Brillouin zone (1st BZ) for woodpile lattices and the directions of the extrinsic magnetic field and wave vector are plotted, respectively. In Figs. 1(a) and (b), gray square columns indicate the function dielectric, which are surrounded by the plasma. One can see from Figs. 1(a) and (b) that each unit cell of the present 3D FPPCs and FMPPCs is composed of four function dielectric square columns layers, and the distance between those four layers is a . For each square columns layer, the inserted columns are parallel, and the interval between two centers of square columns is also a . In those four layers, each layer can be achieved by the upper layer, which is rotated by 90° . It is worth noting that there exists a

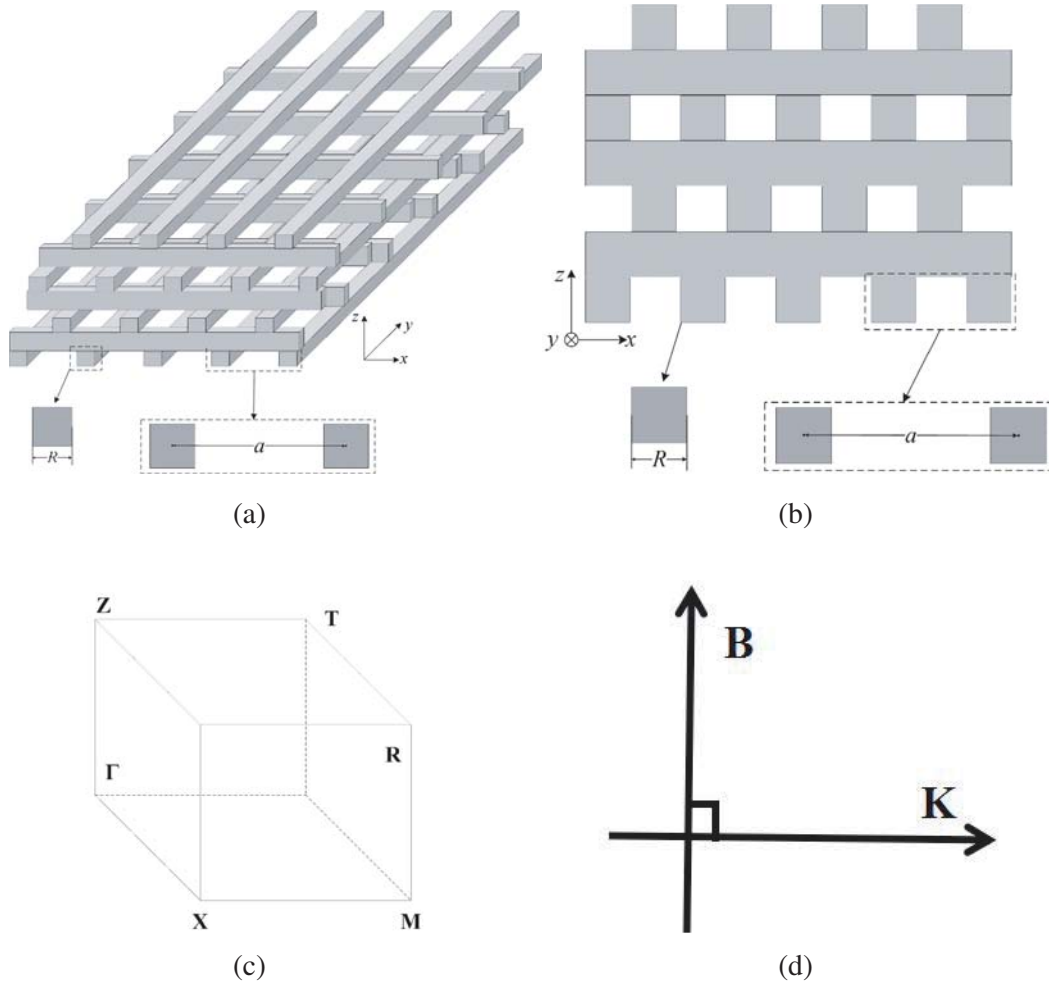


Figure 1. Schematic view of woodpile 3D FPPCs and FMPPCs. (a) Spatial view, (b) side view of woodpile 3D FPPCs and FMPPCs, (c) 1st BZ for the woodpile lattice, and (d) the directions of the extrinsic magnetic field and wave vector.

0.5a movement between the second and fourth layers. A similar phenomenon can also be found in the first and third layers. The details of such a woodpile lattice can be seen in [27–29]. We consider that the length of unit cell is a ; the side length of the square columns is R . ϵ_p and ϵ_a are the permittivities of plasma and inserted square columns, respectively. As mentioned in [45], the symmetry points of woodpile lattices are given in Fig. 1(c). It is well known that if there is no external magnetic field, ϵ_p can be expressed as [5]

$$\epsilon_p = 1 - \frac{\omega_p^2}{\omega^2 + j\nu_c\omega} \tag{1}$$

In Eq. (1), ω_p indicates plasma frequency, and ν_c represents plasma collision frequency. However, if extrinsic magnetic field exists, the directions of the extrinsic magnetic field and wave vector remain vertical at any time as shown in Fig. 1(d). In such a case, the magneto-optical Voigt effect can be found in the magnetized plasma. Therefore, extraordinary and ordinary modes can be observed in the magnetized plasma. As we know [5], for the ordinary mode, the expression of ϵ_p is the same as Eq. (1). For the extraordinary mode, ϵ_p can be written as [5]

$$\epsilon_p = \frac{[\omega(\omega + j\nu_c) - \omega_p^2]^2 - \omega^2\omega_c^2}{\omega^2 [(\omega + j\nu_c)^2 - \omega_c^2] - \omega\omega_p^2(\omega + j\nu_c)} \tag{2}$$

In Eq. (2), ω_c denotes the plasma cyclotron frequency. Obviously, for the 3D FMPPCs case, we only investigate the dispersion curves of the extraordinary mode. In order to achieve the band diagrams of 3D FPPCs and FMPPCs, the plane wave expansion (PWE) method can be used to compute, which is an efficient and accurate method. According to the PWE method, in the reciprocal space, the Maxwell's equation can be simplified as [24–26]:

$$\sum_{\mathbf{G}', \lambda'} |\mathbf{k} + \mathbf{G}| |\mathbf{k} + \mathbf{G}'| \begin{pmatrix} \hat{\mathbf{e}}_2 \cdot \boldsymbol{\varepsilon}_{\mathbf{G}, \mathbf{G}'}^{-1} \cdot \hat{\mathbf{e}}_2' & -\hat{\mathbf{e}}_2 \cdot \boldsymbol{\varepsilon}_{\mathbf{G}, \mathbf{G}'}^{-1} \cdot \hat{\mathbf{e}}_1' \\ -\hat{\mathbf{e}}_1 \cdot \boldsymbol{\varepsilon}_{\mathbf{G}, \mathbf{G}'}^{-1} \cdot \hat{\mathbf{e}}_2' & \hat{\mathbf{e}}_1 \cdot \boldsymbol{\varepsilon}_{\mathbf{G}, \mathbf{G}'}^{-1} \cdot \hat{\mathbf{e}}_1' \end{pmatrix} h_{\mathbf{G}', \lambda'} = \frac{\omega^2}{c^2} h_{\mathbf{G}, \lambda} \quad (3)$$

In Eq. (3), \mathbf{G} is a reciprocal-lattice vector; \mathbf{k} is a wave vector in the BZ; and $\hat{\mathbf{e}}_1$, $\hat{\mathbf{e}}_2$ are orthogonal unit vectors. The derivations and definitions of parametric variables for Eq. (3) can be seen in [24–26]. In Eq. (3), $h_{\mathbf{G}, \lambda}$ can be expressed as [24–26]

$$h_{\mathbf{G}, \lambda} = \sum_{\mathbf{G}} C(\mathbf{k}|\mathbf{G}) e^{j(\mathbf{k}+\mathbf{G}) \cdot \mathbf{r}} \quad (4)$$

The dielectric distributions of such 3D FPPCs and 3D FMPPCs can be satisfied

$$\boldsymbol{\varepsilon}^{-1}(\mathbf{r}) = \begin{cases} \varepsilon_a(\mathbf{r})^{-1} & (\text{in the dielectric columns region}) \\ \varepsilon_p^{-1} & (\text{in the plasma region}) \end{cases} \quad (5a)$$

$$\boldsymbol{\varepsilon}^{-1}(\mathbf{r}) = \begin{cases} \varepsilon_a(\mathbf{r})^{-1} & (\text{in the dielectric columns region}) \\ \varepsilon_p^{-1} & (\text{in the magnetized plasma region}) \end{cases} \quad (5b)$$

Eq. (5) can be written as

$$\boldsymbol{\varepsilon}(\mathbf{r})^{-1} = \varepsilon_p^{-1} + (\varepsilon_a(\mathbf{r})^{-1} - \varepsilon_p^{-1}) \cdot S(\mathbf{r}) \quad (6)$$

where $S(\mathbf{r}) = \begin{cases} 1 & (\text{in the inserted dielectric columns}) \\ 0 & (\text{in the plasma background}) \end{cases}$. Obviously, if Eq. (5) can be computed, the

PBGs of 3D FPPCs and the band structures of the extraordinary mode for the 3D FMPPCs will be achieved. In the following investigations, the permittivity of function dielectric can be expressed as $\varepsilon_a = I \cdot r_1 + b$ [35–37]. I and b are function coefficients, and r_1 is the distance between space ordinate \mathbf{r} (in the inserted square columns) and the central axes of the inserted square columns, respectively. In nature, if the intensity of incident light is space-dependent, the polystyrene and SiO_2 can be considered as the “function dielectric”. It is worth noting that if the form of ε_a is more complicated, Eq. (5) cannot be calculated directly. For instance, $\varepsilon_a = 18 + e^{(5r_1^8)/(r_1^5 + 72r_1^3 + 20)}$. However, this problem can be solved by a method as mentioned in [46]. To compute the PBGs of such FPPCs and FMPPCs, Eqs. (4) and (6) are substituted into Eq. (3). We can obtain

$$\begin{aligned} & \left(\frac{1}{V_{\text{cell}}} \int_{V_{\text{cell}}} \left(\frac{1}{\varepsilon_p} + \left(\frac{1}{\varepsilon_a(\mathbf{r})} - \frac{1}{\varepsilon_p} \right) \cdot S(\mathbf{r}) \right) d\mathbf{r} \right) \cdot \mathbf{E}_1 \cdot \mathbf{E} \cdot C(\mathbf{k}|\mathbf{G}) \\ & + \sum_{\mathbf{G}'} \left(\frac{1}{V_{\text{cell}}} \int_{V_{\text{cell}}} \left(\frac{1}{\varepsilon_p} + \left(\frac{1}{\varepsilon_a(\mathbf{r})} - \frac{1}{\varepsilon_p} \right) \cdot S(\mathbf{r}) \right) \exp(-j\mathbf{G} \cdot \mathbf{r}) d\mathbf{r} \right) \cdot \mathbf{E}_1 \cdot \mathbf{E} \cdot C(\mathbf{k}|\mathbf{G}) = \frac{\omega^2}{c^2} C(\mathbf{k}|\mathbf{G}) \end{aligned} \quad (7)$$

We consider $\mathbf{E} = \begin{bmatrix} \hat{\mathbf{e}}_2 \cdot \hat{\mathbf{e}}_2' & -\hat{\mathbf{e}}_2 \cdot \hat{\mathbf{e}}_1' \\ -\hat{\mathbf{e}}_1 \cdot \hat{\mathbf{e}}_2' & \hat{\mathbf{e}}_1 \cdot \hat{\mathbf{e}}_1' \end{bmatrix}$ and $\mathbf{E}_1 = |\mathbf{k} + \mathbf{G}| |\mathbf{k} + \mathbf{G}'|$. For the 3D FPPCs, Eq. (7) can be written as

$$\zeta^4 \vec{\mathbf{I}} - \zeta^3 \vec{\mathbf{L}} - \zeta^2 \vec{\mathbf{A}} - \zeta \vec{\mathbf{S}} - \vec{\mathbf{D}} = 0 \quad (8)$$

In Eq. (8), $\zeta = \omega/c$, and $\vec{\mathbf{I}}$ is a unit matrix. c is the light speed in vacuum. Thus,

$$\vec{\mathbf{L}}(\mathbf{G}|\mathbf{G}') = -j \frac{\nu_c}{c} \boldsymbol{\delta}_{\mathbf{G}, \mathbf{G}'} \quad (9a)$$

$$\vec{\mathbf{A}}(\mathbf{G}|\mathbf{G}') = \left\{ \frac{\omega_p^2}{c^2} + \vec{\mathbf{O}} \cdot \mathbf{E}_1 \cdot \mathbf{E} \right\} \boldsymbol{\delta}_{\mathbf{G}, \mathbf{G}'} + (\varepsilon_a(r)^{-1} - 1) \vec{\mathbf{P}} \quad (9b)$$

$$\vec{\mathbf{S}}(\mathbf{G}|\mathbf{G}') = \left\{ j \frac{\nu_c}{c} \cdot \vec{\mathbf{O}} \cdot \mathbf{E}_1 \cdot \mathbf{E} \right\} \boldsymbol{\delta}_{\mathbf{G}, \mathbf{G}'} + j \frac{\nu_c}{c} (\varepsilon_a(r)^{-1} - 1) \vec{\mathbf{P}} \quad (9c)$$

$$\vec{\mathbf{D}}(\mathbf{G}|\mathbf{G}') = \left\{ -\frac{\omega_p^2}{c^2} f \varepsilon_a(r)^{-1} \cdot \mathbf{E}_1 \cdot \mathbf{E} \right\} \delta_{\mathbf{G}, \mathbf{G}'} + \frac{\omega_p^2}{c^2} (\varepsilon_a(r)^{-1}) \vec{\mathbf{P}} \quad (9d)$$

where $\vec{\mathbf{P}} = \mathbf{E}_1 \cdot \mathbf{E} \cdot \frac{1}{V_{\text{cell}}} \int_{V_{\text{cell}}} (1 + (\varepsilon_a(\mathbf{r})^{-1} - 1) \cdot S(\mathbf{r})) \exp(-j\mathbf{G} \cdot \mathbf{r}) d\mathbf{r}$ and

$\vec{\mathbf{O}} = \int_{V_{\text{cell}}} (1 + (\varepsilon_a(\mathbf{r})^{-1} - 1) \cdot S(\mathbf{r})) d\mathbf{r}$. In Eq. (9), $\vec{\mathbf{L}}$, $\vec{\mathbf{A}}$, $\vec{\mathbf{S}}$, and $\vec{\mathbf{D}}$ are $N \times N$ matrices. Thus, Eq. (8) can be written in such a form

$$\vec{\mathbf{R}}z = \zeta z, \quad \vec{\mathbf{R}} = \begin{bmatrix} \mathbf{0} & \vec{\mathbf{I}} & \mathbf{0} & \mathbf{0} \\ \mathbf{0} & \mathbf{0} & \vec{\mathbf{I}} & \mathbf{0} \\ \mathbf{0} & \mathbf{0} & \mathbf{0} & \vec{\mathbf{I}} \\ \vec{\mathbf{D}} & \vec{\mathbf{S}} & \vec{\mathbf{A}} & \vec{\mathbf{L}} \end{bmatrix} \quad (10)$$

The band structures can be displayed by solving the eigenvalues of Eq. (10). How to calculate $\varepsilon_{\mathbf{G}, \mathbf{G}'}^{-1}$ can be seen in [47, 48]. Similarly, for 3D MFPPCs, Eq. (7) can also be expressed as

$$\zeta^6 \mathbf{I} - \zeta^5 \vec{\mathbf{L}} - \zeta^4 \vec{\mathbf{A}} - \zeta^3 \vec{\mathbf{S}} - \zeta^2 \vec{\mathbf{D}} - \zeta \vec{\mathbf{Z}} - \vec{\mathbf{X}} = 0 \quad (11)$$

In Eq. (11), ζ , \mathbf{I} and c are similar to those in Eq. (9). Thus,

$$\mathbf{L}(\mathbf{G}|\mathbf{G}') = -j \frac{2\nu_c}{c} \delta_{\mathbf{G}, \mathbf{G}'}, \quad (12a)$$

$$\mathbf{A}(\mathbf{G}|\mathbf{G}') = j \left(\frac{2\omega_p^2 + \omega_c^2 + \nu_c^2}{c^2} \right) \delta_{\mathbf{G}, \mathbf{G}'} + \mathbf{M} + \mathbf{N}, \quad (12b)$$

$$\mathbf{S}(\mathbf{G}|\mathbf{G}') = j \left(\frac{2\nu_c \omega_p^2}{c^3} + \frac{2\nu_c}{c} (\mathbf{M} + \mathbf{N}) \right), \quad (12c)$$

$$\mathbf{D}(\mathbf{G}|\mathbf{G}') = - \left((\mathbf{M} + \mathbf{N}) \left(\frac{\nu_c^2 + \omega_c^2}{c^2} \right) + \frac{\omega_p^2}{c^2} (2\mathbf{N} + \mathbf{M}) + \frac{\omega_p^4}{c^4} \delta_{\mathbf{G}, \mathbf{G}'} \right), \quad (12d)$$

$$\mathbf{Z}(\mathbf{G}|\mathbf{G}') = -j \frac{\nu_c \omega_p^2}{c^3} (\mathbf{N} + \mathbf{M}), \quad (12e)$$

$$\mathbf{X}(\mathbf{G}|\mathbf{G}') = \frac{\omega_p^4}{c^4} \mathbf{N}, \quad (12f)$$

where $\mathbf{M} = (\mathbf{O} \cdot \mathbf{E}_1 \cdot \mathbf{E}) \delta_{\mathbf{G}, \mathbf{G}'} + (\varepsilon_a(r)^{-1} - 1) \mathbf{P}$, $\mathbf{N} = ((\mathbf{O} - f \varepsilon_a(r)^{-1}) \cdot \mathbf{E}_1 \cdot \mathbf{E}) \delta_{\mathbf{G}, \mathbf{G}'} + (2\varepsilon_a(r)^{-1} - 1) \mathbf{P}$, f is filling factor of dielectric square columns, $\mathbf{P} = \mathbf{E}_1 \cdot \mathbf{E} \cdot \frac{1}{V_{\text{cell}}} \int_{V_{\text{cell}}} (1 + (\varepsilon_a(\mathbf{r})^{-1} - 1) \cdot S(\mathbf{r})) \exp(-j\mathbf{G} \cdot \mathbf{r}) d\mathbf{r}$ and $\mathbf{O} = \int_{V_{\text{cell}}} (1 + (\varepsilon_a(\mathbf{r})^{-1} - 1) \cdot S(\mathbf{r})) d\mathbf{r}$. In Eq. (12), \mathbf{L} , \mathbf{A} , \mathbf{S} , \mathbf{D} , \mathbf{X} and \mathbf{Z} are $N \times N$ matrices. Thus, Eq. (11) can be expressed as in the following form

$$\mathbf{R}z = \zeta z, \quad \mathbf{R} = \begin{bmatrix} \mathbf{0} & \mathbf{I} & \mathbf{0} & \mathbf{0} & \mathbf{0} & \mathbf{0} \\ \mathbf{0} & \mathbf{0} & \mathbf{I} & \mathbf{0} & \mathbf{0} & \mathbf{0} \\ \mathbf{0} & \mathbf{0} & \mathbf{0} & \mathbf{I} & \mathbf{0} & \mathbf{0} \\ \mathbf{0} & \mathbf{0} & \mathbf{0} & \mathbf{0} & \mathbf{I} & \mathbf{0} \\ \mathbf{0} & \mathbf{0} & \mathbf{0} & \mathbf{0} & \mathbf{0} & \mathbf{I} \\ \mathbf{X} & \mathbf{Z} & \mathbf{D} & \mathbf{S} & \mathbf{A} & \mathbf{L} \end{bmatrix} \quad (13)$$

Obviously, the PBGs for the extraordinary mode of 3D FMPPCs can be obtained by the calculation results of Eq. (13).

3. NUMERICAL RESULTS AND DISCUSSIONS

To obtain the dispersion diagrams, 2197 plane waves are introduced into the PWE method [48], and the unit cell is divided into $250 \times 250 \times 250$ cubes [46]. A constant $\omega_{p0} = 2\pi c/a$ is used to normalize

the frequency region, ω_p and ν_c . As the initial values, $\omega_p = 0.12\omega_{p0}(\omega_{pm})$ and $\nu_c = 0.002\omega_p(\nu_{cm})$, respectively. We also assume that $I = 35$, $b = 18$ and $R = 0.125a$, respectively.

In Fig. 2, when $R = 0.125a$, the PCs dispersion diagrams with different parameters are displayed. The red regions represent the PBGs. It can be seen from Figs. 2(a) and (b) that when $\omega_p = \nu_c = 0$, the present PCs can be looked as the 3D dielectric-air PCs since $\varepsilon_p = 1$. As shown in Fig. 2(a) (the case of $I = 0$), a PBG can be seen in the dispersion diagram, which runs from 0.331049 to 0.415156 ($2\pi c/a$). When $I = 35$ (see Fig. 2(b)), the frequency region of PBG will move to the lower frequencies, which covers 0.307608–0.392138 ($2\pi c/a$). Compared with Fig. 2(a), enhanced PBG can be obtained since I increases. As shown in Fig. 2(c), when $\omega_p = \omega_{pm}$, $\nu_c = \nu_{cm}$ and $\varepsilon_a = 18$, the PBG of 3D FPPCs spans from 0.333706 to 0.421793 ($2\pi c/a$), and an FBR can be seen in the band structures, which covers 0–0.12 ($2\pi c/a$). As we know [24–26], the FBR stems from the surface plasma wave, which can be localized around the embedded dielectric square columns. Compared with the results in Fig. 2(a), the edges of PBG shift to the higher frequencies, and its bandwidth is enlarged by 0.004 ($2\pi c/a$). Similar trend can also be found in [24–26]. One can see from Fig. 2(d) that when $I = 35$, the PBG of 3D FPPCs will be located at 0.310147–0.398306 ($2\pi c/a$), whose frequency range will be changed to 0.0882 ($2\pi c/a$). Compared with Fig. 2(c), the PBG will redshift. The bandwidth of PBG increases obviously compared with that in Figs. 2(b) and (c). Evidently, the maximum bandwidth of PBG can be seen in

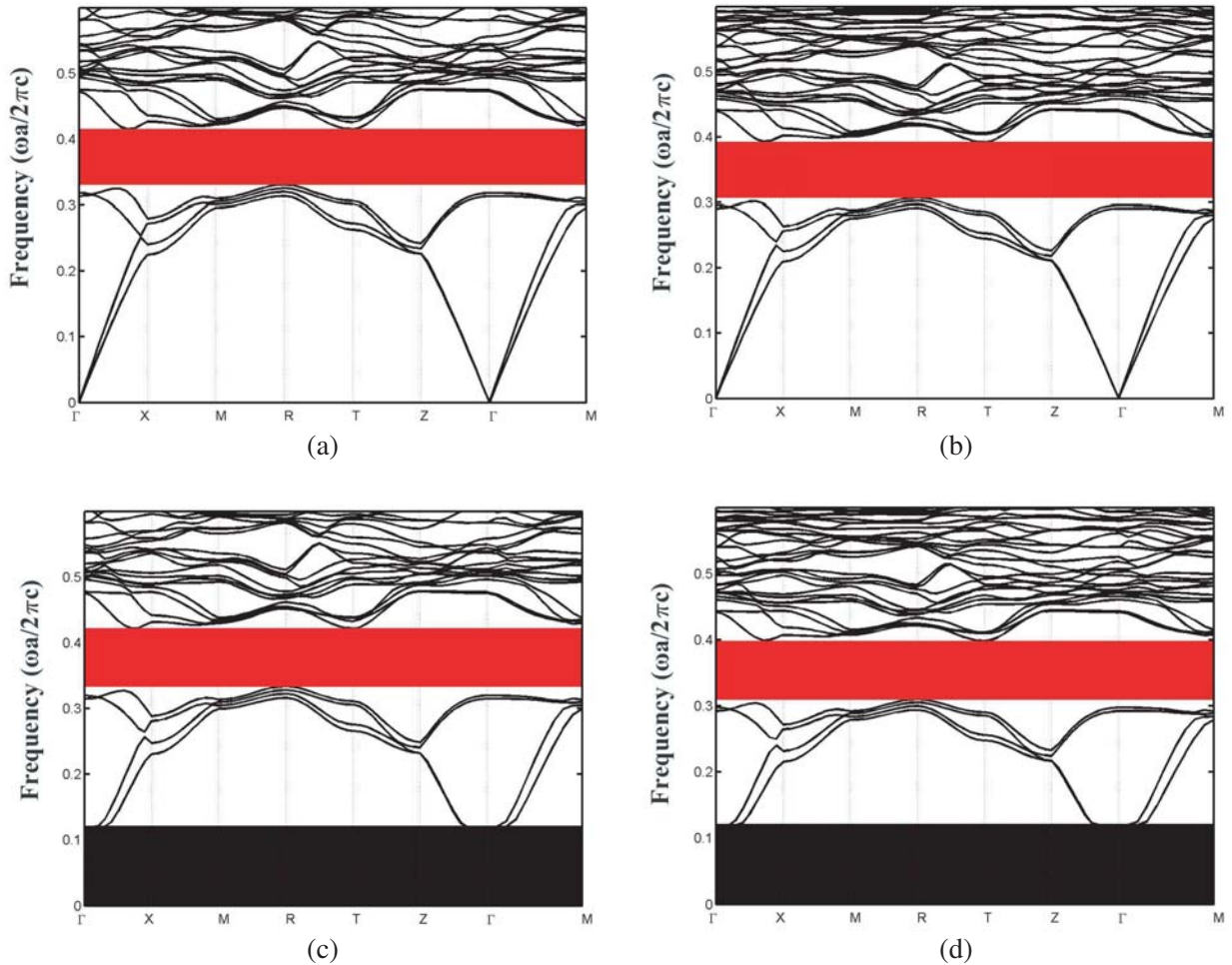


Figure 2. The PCs dispersion diagrams with different parameters when $R = 0.125a$. (a) $\omega_p = \nu_c = 0$, $\varepsilon_a = 18$, (b) $\omega_p = \nu_c = 0$, $\varepsilon_a = 35r_1 + 18$, (c) $\omega_p = \omega_{pm}$, $\nu_c = \nu_{cm}$, $\varepsilon_a = 18$, (d) $\omega_p = \omega_{pm}$, $\nu_c = \nu_{cm}$, $\varepsilon_a = 35r_1 + 18$.

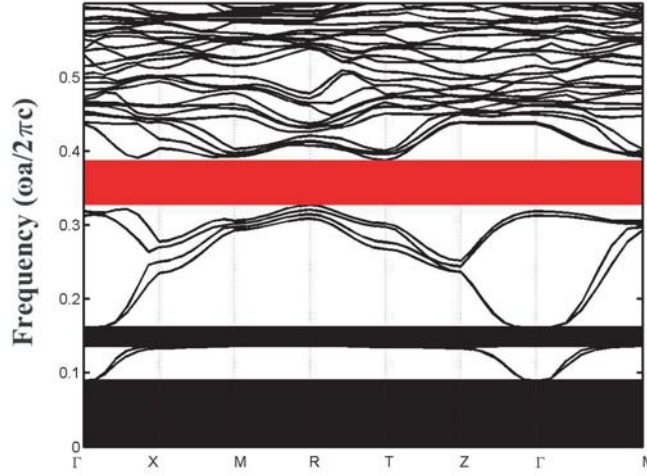


Figure 3. The dispersion diagram for the extraordinary mode of 3D FMPPCs when $R = 0.125a$, $\omega_p = \omega_{pm}$, $\omega_c = \omega_{cm}$, $\nu_c = \nu_{cm}$ and $\varepsilon_a = 35r_1 + 18$.

Fig. 2(d) compared with Figs. 2(a)–(c). In Fig. 3, the dispersion diagram for the extraordinary mode of 3D FMPPCs is plotted, when $R = 0.125a$, $\omega_p = \omega_{pm}$, $\omega_c = \omega_{cm}$, $\nu_c = \nu_{cm}$ and $\varepsilon_a = 35r_1 + 18$. As shown in Fig. 3, there exists a PBG, which covers $0.327429\text{--}0.387588$ ($2\pi c/a$). Besides, there are two FBRs. The first FBR runs from 0 to 0.0893 ($2\pi c/a$), and the second FBR spans from 0.1399 to 0.1613 ($2\pi c/a$). In magneto-optical Voigt effect, the locations of edges of such two FBRs are determined by the values of f_L , f_U and f_R [19–21], which are $f_L = -\omega_c^2/2 + \sqrt{\omega_c^2/4 + \omega_p^2}$, $f_U = \sqrt{\omega_c^2 + \omega_p^2}$, and $f_R = \omega_c^2/2 + \sqrt{\omega_c^2/4 + \omega_p^2}$, respectively. Obviously, the bandwidth of PBG for the extraordinary mode is narrowed compared with Fig. 2(d). According to the results in Figs. 2 and 3, we can find that the smallest PBG can be seen in Fig. 3, whose frequency range is 0.060159 ($2\pi c/a$). Compared with the 3D function dielectric PCs and 3D plasma-dielectric PCs with the same lattices (see Figs. 2(b) and (d)), narrower PBG for the extraordinary mode can be obtained in the proposed FMPPCs. However, for the present 3D FPPCs, compared with 3D dielectric-air PCs, 3D function dielectric PCs and 3D plasma-dielectric PCs with the same topology, wider bandwidth of PBG can be obtained. In the following, the relationships between the parameters of proposed FPPCs and FMPPCs and the features of the PBGs for the extraordinary mode and electromagnetic wave will be investigated. For convenience, PBG of FMPPCs is used to specifically refer to the PBG for the extraordinary mode. We consider that the relative bandwidth of PBG is $\delta\omega/\omega_i$ and that $\delta\omega$ is the frequency range of a PBG, and ω_i indicates the center frequency of a PBG.

3.1. The Effects I on the PBGs for the Proposed FPPCs and FMPPCs

The curves of I vs. PBG and I vs. $\delta\omega/\omega_i$ of the 3D FPPCs and FMPPCs with different I are plotted in Figs. 4 and 5, respectively, when $\omega_p = \omega_{pm}$, $\nu_c = \nu_{cm}$, $\omega_c = \omega_{cm}$, $R = 0.125a$ and $\varepsilon_a = I \cdot r_1 + 18$. We can see from Figs. 4(a) and 5(a) that the locations of PBGs can be tailored obviously by altering the value of I . The edges of PBGs for the 3D FPPCs and FMPPCs will redshift when I increases, whose frequency regions are increased first and then decreased. As shown in Fig. 4(a), when $I = -90, -10, 10$ and 90 , the PBGs are located at $0.421753\text{--}0.484965$ ($2\pi c/a$), $0.312752\text{--}0.394422$ ($2\pi c/a$), $0.297121\text{--}0.378644$ ($2\pi c/a$) and $0.252601\text{--}0.326038$ ($2\pi c/a$), whose bandwidths are 0.0632 ($2\pi c/a$), 0.0817 ($2\pi c/a$), 0.0815 ($2\pi c/a$) and 0.0734 ($2\pi c/a$), respectively. Obviously, the PBG is widened first and then narrowed with the increasing value of I . The largest PBG can be seen in the case of $I = -5$, which is 0.08169 ($2\pi c/a$). Compared with the case of $I = -90$, the frequency region of PBG is enhanced by 0.01849 ($2\pi c/a$). Such a phenomenon can be explained. Increasing I means that the averaged refractive index of FPPCs increases [3]. Thus, the PBG of the 3D FPPCs can be adjusted by I . A similar trend can also be found

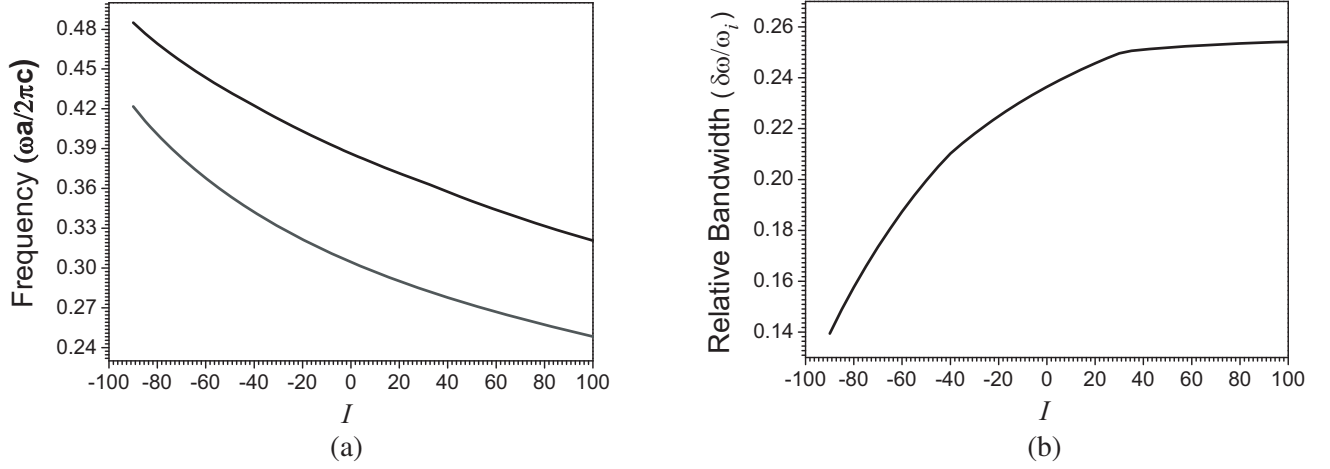


Figure 4. The curves of I vs. PBG and I vs. $\delta\omega/\omega_i$ of the 3D FPPCs, (a) the curve of I vs. PBG; (b) the curve of I vs. $\delta\omega/\omega_i$.

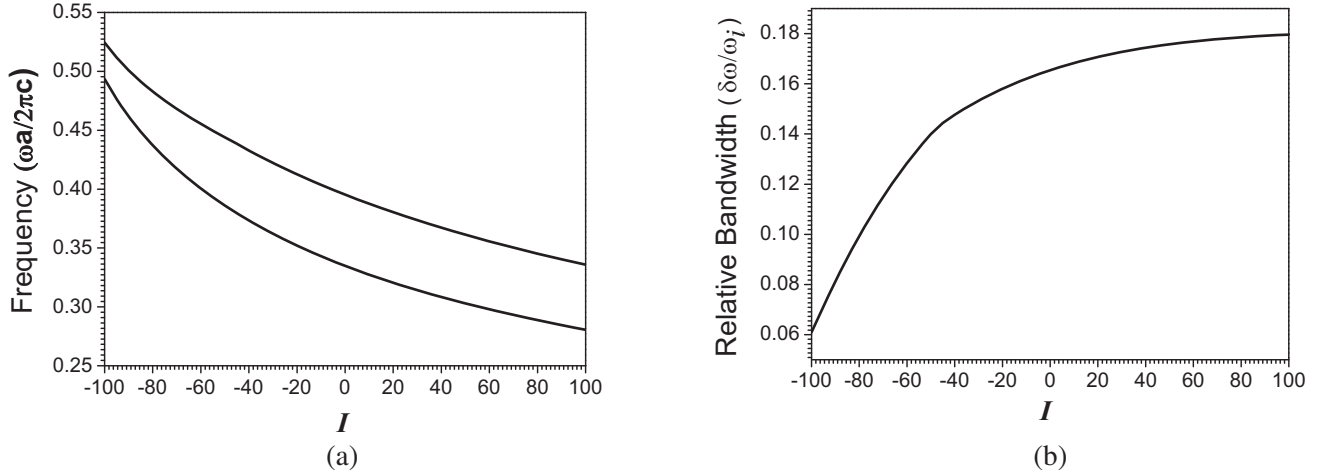


Figure 5. The curves of I vs. PBG and I vs. $\delta\omega/\omega_i$ of the 3D FMPPCs, (a) the curve of I vs. PBG; (b) the curve of I vs. $\delta\omega/\omega_i$.

in Fig. 5(a). When $I = -100, -60, -20$ and 20 , the PBGs cover $0.49343\text{--}0.52444$ ($2\pi c/a$), $0.40041\text{--}0.45535$ ($2\pi c/a$), $0.35213\text{--}0.41256$ ($2\pi c/a$) and $0.32056\text{--}0.38037$ ($2\pi c/a$), whose frequency regions are 0.03101 ($2\pi c/a$), 0.05494 ($2\pi c/a$), 0.06043 ($2\pi c/a$) and 0.05981 ($2\pi c/a$), respectively. Obviously, the PBG will be narrowed as I is changed from -20 to 20 . For the 3D FMPPCs, the largest PBG can be found in the case of $I = -10$, whose bandwidth is 0.0605 ($2\pi c/a$). Larger I may lead to narrower PBG. However, different trends can be seen in Figs. 4(b) and 5(b). For the 3D FPPCs and FMPPCs, $\delta\omega/\omega_i$ are proportional to the increasing value of I . The maximum $\delta\omega/\omega_i$ can be obtained in the case of $I = 100$ for those two cases, whose values are 0.25413 and 0.17959 , respectively. Compared with the case of $I = -100$, the increase of 0.1147 and 0.1187 can be achieved in Figs. 4(b) and 5(b), respectively. It needs to be noticed that the FBRs of 3D FPPCs and FMPPCs will remain unchanged as I is altered. This is because the locations of FBRs are determined by the values of ω_p and ω_c [19–21].

3.2. The Effects b on the PBGs for the Proposed FPPCs and FMPPCs

The curves of b vs. PBG and b vs. $\delta\omega/\omega_i$ of the 3D FPPCs and FMPPCs with different b are displayed in Figs. 6 and 7, respectively, when $\omega_p = \omega_{pm}$, $\nu_c = \nu_{cm}$, $\omega_c = \omega_{cm}$, $R = 0.125a$ and $\varepsilon_a = 35 \cdot r_1 + b$.

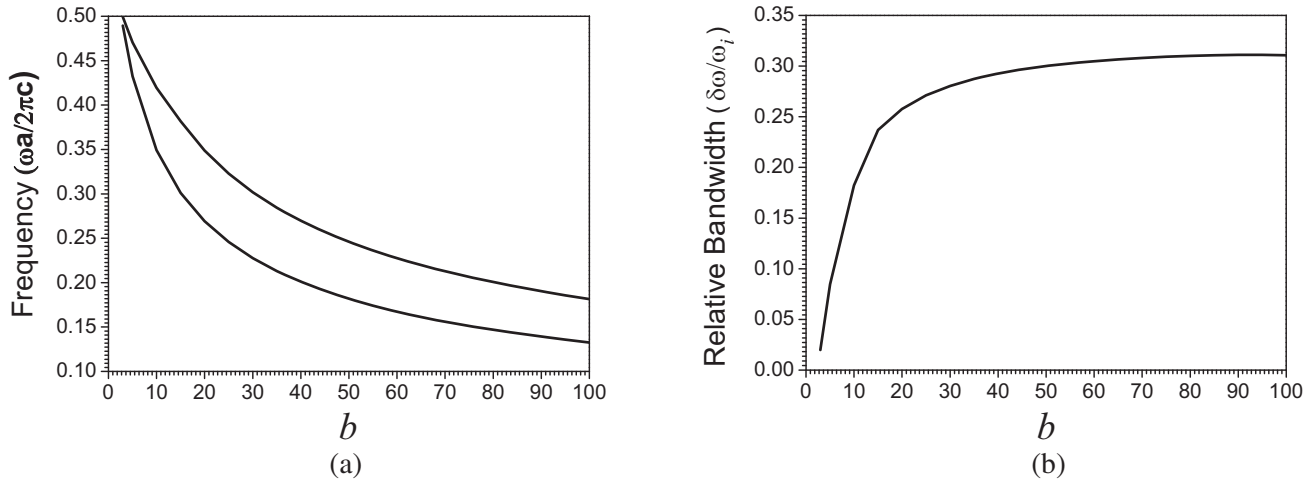


Figure 6. The curves of b vs. PBG and b vs. $\delta\omega/\omega_i$, (a) the curve of b vs. PBG; (b) the curve of b vs. $\delta\omega/\omega_i$.

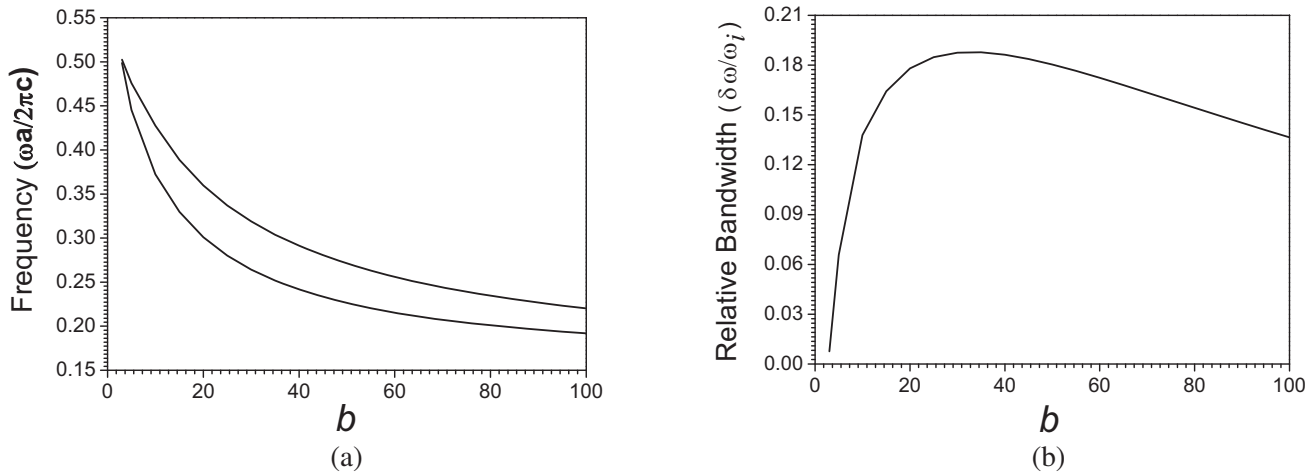


Figure 7. The curves of b vs. PBG and b vs. $\delta\omega/\omega_i$, (a) the curve of b vs. PBG; (b) the curve of b vs. $\delta\omega/\omega_i$.

As shown in Figs. 6(a) and 7(a), the PBGs for the 3D FPPCs and FMPPCs can be tuned when b increases. The edges of those PBGs shift to the lower frequencies, and their bandwidths increase first and then decrease. Obviously, the larger b will result in a PBG in the lower frequencies. It can be seen from Fig. 6(a) that when b is less than 3, such a PBG will not exist. When $b = 5, 15, 65$ and 95 , the PBGs for the 3D FPPCs cover $0.432263\text{--}0.470576$ ($2\pi c/a$), $0.300977\text{--}0.381889$ ($2\pi c/a$), $0.161387\text{--}0.219828$ ($2\pi c/a$) and $0.135707\text{--}0.185684$ ($2\pi c/a$), whose bandwidths are 0.038313 , 0.080912 ($2\pi c/a$), 0.058441 ($2\pi c/a$) and 0.049977 ($2\pi c/a$), respectively. Evidently, with the increasing value of b , the PBG is enhanced first and then narrowed. The maximum PBG appears in the case of $b = 5$. The similar changing trend can also be seen in Fig. 7(a). For 3D FMPPCs, when b is changed from 35 to 45, the frequency region of PBG is changed from $0.25173\text{--}0.30389$ ($2\pi c/a$) to $0.23333\text{--}0.28052$ ($2\pi c/a$), which is decreased by 0.00497 ($2\pi c/a$). The largest PBG can also be obtained when $b = 15$. It can be seen from Fig. 6(b) that when b increases, the values of $\delta\omega/\omega_i$ of PBGs for 3D FPPCs increase. For 3D FPPCs, when $b = 100$, the largest $\delta\omega/\omega_i$ can be gotten, which is 0.31059 . When b is altered from 3 to 100, $\delta\omega/\omega_i$ is enhanced by 0.2908 . For 3D MFPPCs (see Fig. 7(b)), when b increases, $\delta\omega/\omega_i$ increases first then decreases. The maximum $\delta\omega/\omega_i$ is 0.18774 , which can be seen in the case of $b = 35$. If b is changed from 3 to 35, $\delta\omega/\omega_i$ is enhanced by 0.18013 . As mentioned above, for those two PBGs, the

reconfigure frequency regions are every large if b can be tuned obviously. Those two widened PBGs can be achieved by optimizing the value of b , and larger PBG will appear in the low- b region.

3.3. The Effects ω_p on the PBGs for the Proposed FPPCs and FMPPCs

The curves of ω_p vs. PBG and ω_p vs. $\delta\omega/\omega_i$ of the 3D FPPCs and FMPPCs with different ω_p are given in Figs. 8 and 9, respectively, when $\nu_c = \nu_{cm}$, $\omega_c = \omega_{cm}$, $R = 0.125a$ and $\varepsilon_a = 35 \cdot r_1 + 18$. As shown in Figs. 8(a) and 9(a), the locations and regions of PBGs for the 3D FPPCs and FMPPCs can be tailored obviously when ω_p is changed. The edges of those PBGs will blueshift. As shown in Fig. 8(a), for 3D FPPCs, when ω_p increases, the bandwidth of PBG will increase first and then decrease. When ω_p/ω_{p0} increases from 0.1 to 0.26, the largest PBG can be seen in the case of $\omega_p/\omega_{p0} = 0.26$, whose bandwidth is $0.08628 (2\pi c/a)$, and the frequency region of PBG is enhanced by $0.0067 (2\pi c/a)$. When $\omega_p/\omega_{p0} = 0.02, 0.1, 0.18$ and 0.26 , the PBGs are located at $0.278627\text{--}0.356294 (2\pi c/a)$, $0.279996\text{--}0.359579 (2\pi c/a)$, $0.283678\text{--}0.367136 (2\pi c/a)$ and $0.293031\text{--}0.379312 (2\pi c/a)$, respectively. Obviously, the PBG is broadened. If the value of ω_p continues to increase, the PBG will be narrowed. For

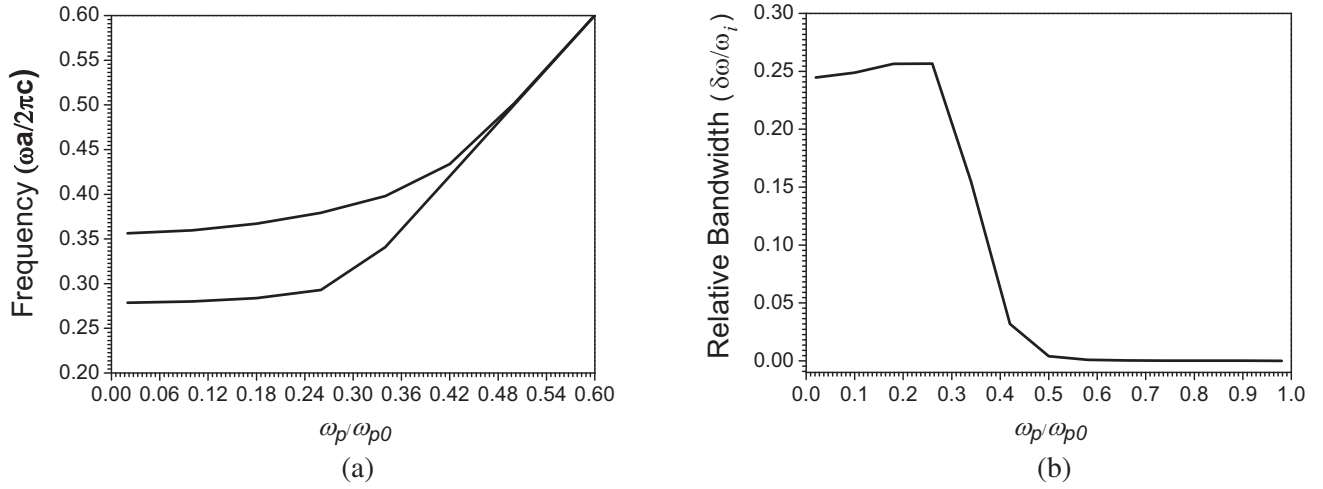


Figure 8. The curves of ω_p vs. PBG and ω_p vs. $\delta\omega/\omega_i$, (a) the curve of ω_p vs. PBG; (b) the curve of ω_p vs. $\delta\omega/\omega_i$.

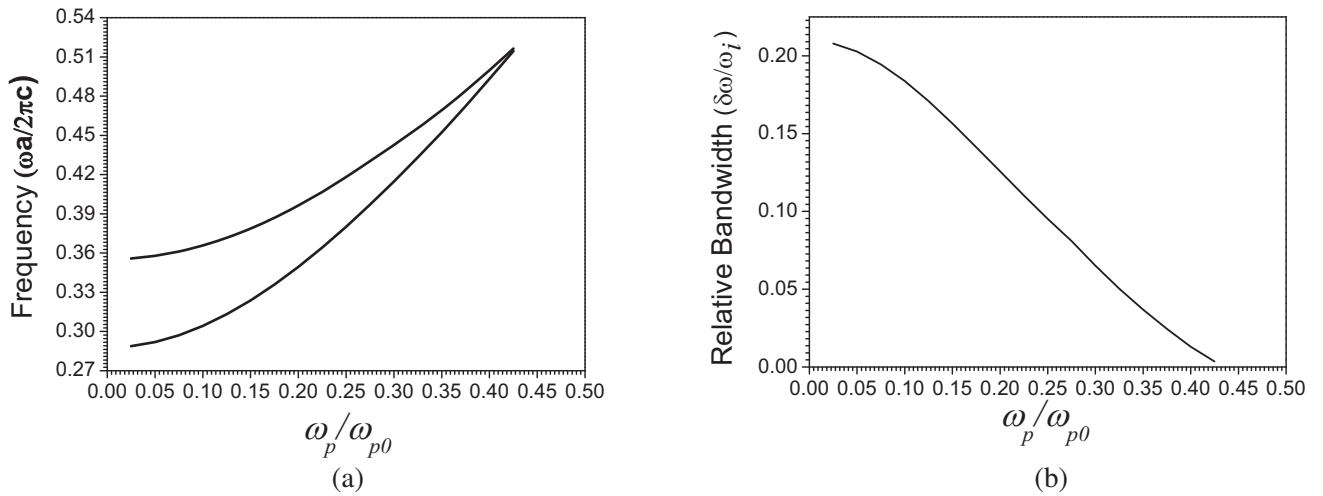


Figure 9. The curves of ω_p vs. PBG and ω_p vs. $\delta\omega/\omega_i$, (a) the curve of ω_p vs. PBG; (b) the curve of ω_p vs. $\delta\omega/\omega_i$.

instance, when ω_p/ω_{p0} is changed from 0.34 to 0.42, the covered region of PBG is altered from 0.340851–0.397956 ($2\pi c/a$) to 0.420147–0.433736 ($2\pi c/a$), and its frequency range is decreased by 0.0435 ($2\pi c/a$). If $\omega_p/\omega_{p0} > 0.5$, the PBG will be gradually narrowed. If $\omega_p/\omega_{p0} > 0.6$, the PBG will disappear. The different phenomenon can be seen in Fig. 9(a). Fig. 9(a) shows that the frequency region of PBG decreases as the edges blueshift. When $\omega_p/\omega_{p0} = 0.025, 0.1, 0.2$ and 0.4 , the PBGs for the 3D MFPPCs cover 0.28878–0.35578 ($2\pi c/a$), 0.30422–0.36577 ($2\pi c/a$), 0.34944–0.39632 ($2\pi c/a$), and 0.49321–0.49968 ($2\pi c/a$), respectively, and its frequency range is decreased by 0.06053 ($2\pi c/a$). When $\omega_p/\omega_{p0} = 0.025$, the maximum PBG can be seen, whose bandwidth is 0.20789 ($2\pi c/a$). When ω_p/ω_{p0} increases from 0.025 to 0.425, the bandwidth of PBG is decreased by 0.2044 ($2\pi c/a$). If $\omega_p/\omega_{p0} > 0.425$, the PBG will disappear. According to the results in Figs. 8(a) and 9(a), we can know that the requirement of a larger value of ω_p is not necessary to achieve larger PBGs for the 3D FPPCs and FMPPCs. As shown in Fig. 8(a), for 3D FPPCs, $\delta\omega/\omega_i$ will increase first and then decrease as ω_p/ω_{p0} increases. When ω_p/ω_{p0} is equal to 0.26, the largest $\delta\omega/\omega_i$ can be gotten, which is 0.25666. Compared with the case of $\omega_p/\omega_{p0} = 0.1$, $\delta\omega/\omega_i$ is enhanced by 0.0078. However, the different curve can be seen in Fig. 9(b). For 3D MFPPCs, $\delta\omega/\omega_i$ will decrease nearly linearly with the increasing value of ω_p/ω_{p0} . When ω_p/ω_{p0} increases to 0.425, the minimum $\delta\omega/\omega_i$ can be achieved, which is 0.00353. Compared with the case of $\omega_p/\omega_{p0} = 0.125$, $\delta\omega/\omega_i$ is decreased by 0.1674. Consequently, the PBGs for those two cases can be adjusted by ω_p , which is an important parameter to enhance the PBGs, and larger PBGs appear in the low- ω_p region. The upper edges of FBRs for those two cases linearly increase as ω_p increases. Thus, the enhanced PBGs of those two cases can be realized by tailoring ω_p in a suitable value.

3.4. The Effects R on the PBGs for the Proposed FPPCs and FMPPCs

The curves of R vs. PBG and R vs. $\delta\omega/\omega_i$ of the 3D FPPCs and FMPPCs with different R are present in Figs. 10 and 11, respectively, when $\omega_p = \omega_{pm}$, $\nu_c = \nu_{cm}$, $\omega_c = \omega_{cm}$ and $\varepsilon_a = 35 \cdot r_1 + 18$. In both cases, the locations of central axes of each layer of inserted dielectric square columns are never changed, but only the value of R is changed. As shown in Figs. 10(a) and 11(a), R is a key parameter to adjust the PBGs. We can see from Fig. 10(a) that when $R = 0.11125a, 0.1125a$ and $0.11375a$, the areas of the PBG are altered to 0.402396–0.439993 ($2\pi c/a$), 0.358022–0.429001 ($2\pi c/a$) and 0.402655–0.440035 ($2\pi c/a$), respectively. The edges of PBG will redshift first and then blueshift. The bandwidth of PBG also is widened first and then decreases. The general trend of the curve is that the edges of PBG will redshift. For the lower edge of PBG, there exist some trip points, such as $R = 0.11125a, R = 0.11375a$ and $R = 0.11875a$. The largest PBG can be found in the case of $R = 0.12375a$, which covers 0.32511–0.41823 ($2\pi c/a$). If R is varied from 0.10125a to 0.12375a, the region of PBG is enhanced by 0.0836 ($2\pi c/a$). We can see from Fig. 11(a) that the covered region of PBG is downward to the lower

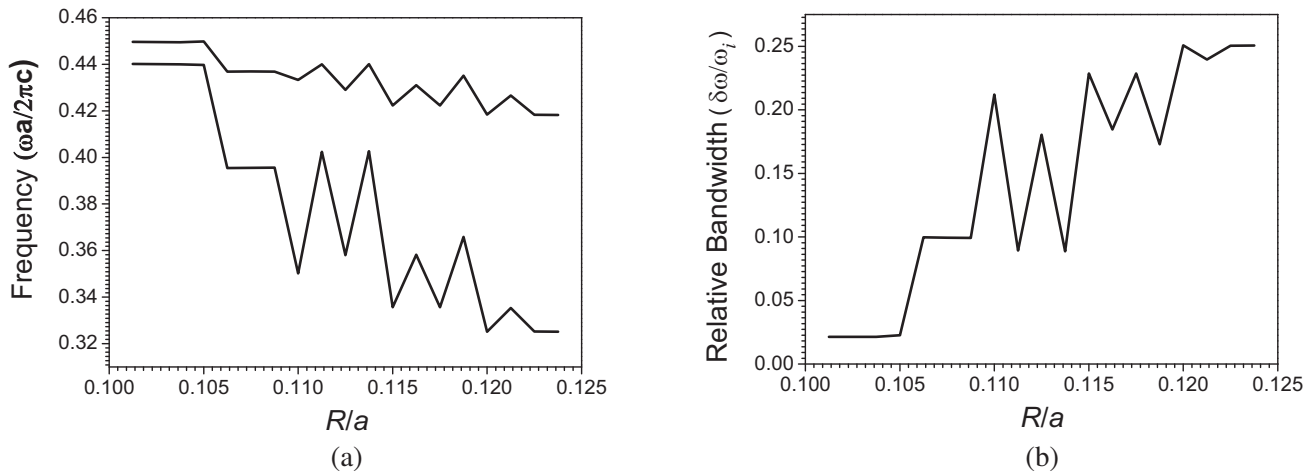


Figure 10. The curves of R vs. PBG and R vs. $\delta\omega/\omega_i$, (a) the curve of R vs. PBG; (b) the curve of R vs. $\delta\omega/\omega_i$.

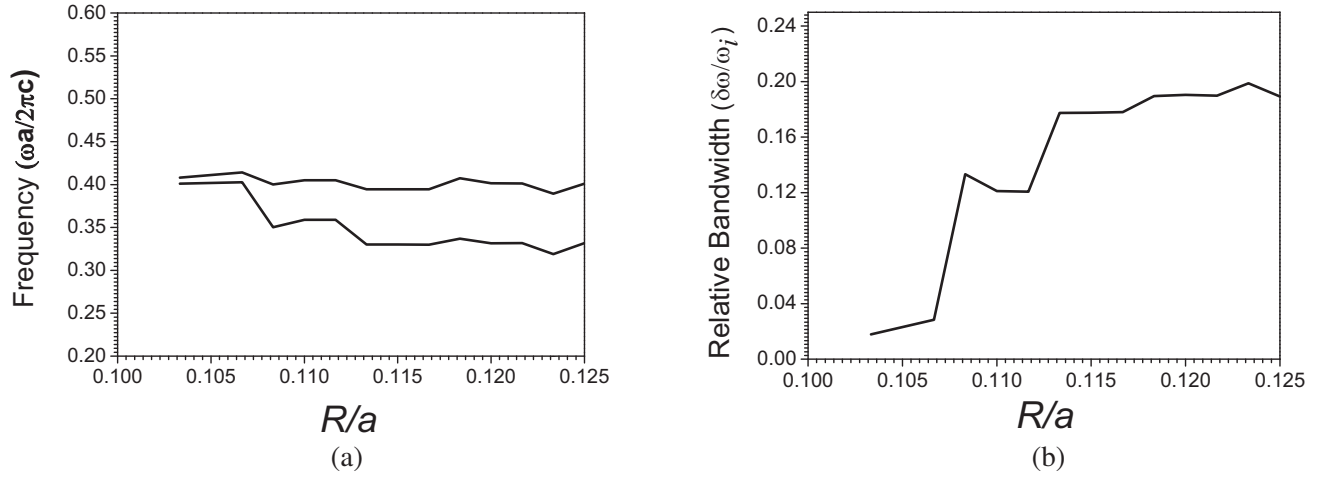


Figure 11. The curves of R vs. PBG and R vs. $\delta\omega/\omega_i$, (a) the curve of R vs. PBG; (b) the curve of R vs. $\delta\omega/\omega_i$.

frequencies when R increases, and its bandwidth also generally increases. The upper edge of PBG will almost remain unchanged at frequency $0.4(2\pi c/a)$. However, for the lower edge of PBG, the different trend can be seen, in which the obvious redshift can be observed. When $R = 0.1033a$, $0.1067a$, $0.1083a$ and $0.1133a$, the covered regions of PBGs will be $0.40094\text{--}0.40816$ ($2\pi c/a$), $0.40263\text{--}0.41424$ ($2\pi c/a$), $0.35017\text{--}0.40014$ ($2\pi c/a$) and $0.33014\text{--}0.39443$ ($2\pi c/a$), respectively, whose bandwidth is enhanced by 0.0633 ($2\pi c/a$). As shown in Fig. 10(b), for 3D FPPCs, $\delta\omega/\omega_i$ increases when R increases except for some trip points. When $R = 0.12375a$, the largest $\delta\omega/\omega_i$ can be gotten, which is 0.25053 . If R/a is varied from $0.10125a$ to $0.12375a$, $\delta\omega/\omega_i$ increases by 0.2292 . Obviously, if we want to obtain a larger PBG, the value of R/a has to be large (in the high- R region). As shown in Fig. 11(b), for 3D MFPPCs, $\delta\omega/\omega_i$ maintains a general growth trend as R becomes larger. The largest $\delta\omega/\omega_i$ can be found in the case of $R = 0.1233a$, which is 0.07041 . If R/a is varied from $0.1033a$ to 0.125 , $\delta\omega/\omega_i$ is enhanced by 0.0621 . Obviously, if we want to obtain a larger PBG for those two cases, the value of R/a has to be a large one. This can be explained by that the larger R/a means that the average refractive indices of those PCs are larger enough to open a larger PBG [2].

3.5. The Effects ω_c on the PBG for the Proposed FMPPCs

The curves of ω_c vs. PBG and ω_c vs. $\delta\omega/\omega_i$ of the 3D FMPPCs with different ω_c are plotted in Fig. 12, respectively, when $\omega_p = \omega_{p1} = \omega_{pm}$, $\nu_c = \nu_{cm}$, $R = 0.125a$ and $\varepsilon_a = 35 \cdot r_1 + 18$. We can see from Fig. 12(a) that the edges and frequency region of PBG can be manipulated by ω_c . When ω_c increases, the blueshift can be observed in the edges of PBG, and the area of PBG decreases slightly. When ω_c/ω_{p1} is changed from 0.1 to 0.4 , the regions of PBGs cover $0.30984\text{--}0.36976$ ($2\pi c/a$), $0.30995\text{--}0.36981$ ($2\pi c/a$) and $0.31042\text{--}0.37002$ ($2\pi c/a$), respectively. Obviously, the frequency region of PBG is enhanced by 0.00032 ($2\pi c/a$). If the value of ω_c continues to increase, the bandwidth of PBG will decrease. When ω_c/ω_{p1} is equal to 0.6 , 0.8 and 1 , the regions of PBGs cover $0.31123\text{--}0.37038$ ($2\pi c/a$), $0.31245\text{--}0.37091$ ($2\pi c/a$) and $0.31417\text{--}0.37164$ ($2\pi c/a$), respectively, and its bandwidth is decreased by 0.0017 ($2\pi c/a$). Therefore, the bandwidth of PBG becomes smaller than the case of $\omega_c/\omega_{p1} = 0.6$. If $\omega_c/\omega_{p1} = 0.1$, the maximum PBG can be obtained, whose frequency area is 0.05993 ($2\pi c/a$). When ω_c/ω_{p1} increases from 0.1 to 3.25 , the bandwidth of PBG is decreased by 0.0532 ($2\pi c/a$). If $\omega_c/\omega_{p1} > 2$, the region of PBG will drastically decrease. If $\omega_c/\omega_{p1} > 3.5$, the PBG will not exist. As mentioned above, we can know that a larger PBG can be achieved with a smaller value of ω_c/ω_{p1} . On the other hand, as shown in Fig. 10(b), if ω_c/ω_{p1} has a larger value, $\delta\omega/\omega_i$ will decrease drastically. If ω_c/ω_{p1} increases from 0.1 to 3.25 , the minimum $\delta\omega/\omega_i$ can be obtained in the case of $\omega_c/\omega_{p1} = 3.25$, which is 0.01538 . Compared with the maximum value, $\delta\omega/\omega_i$ is decreased by 0.161 . Obviously, the PBG can be tailored by altering the value of ω_c , and the larger PBG can be found in the low- ω_c region.

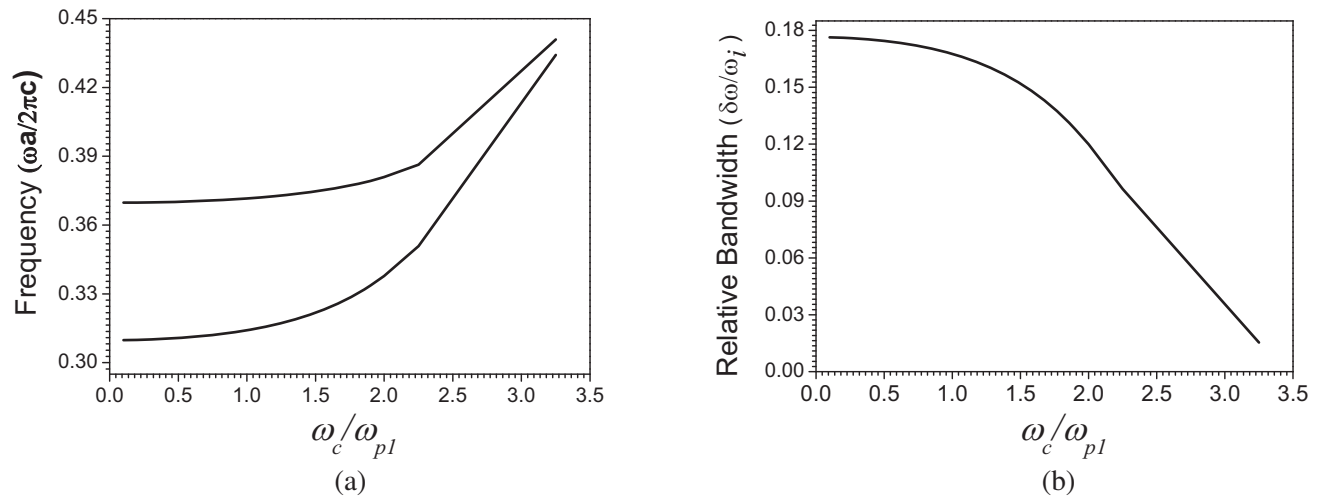


Figure 12. The curves of ω_c vs. PBG and ω_c vs. $\delta\omega/\omega_i$, (a) the curve of ω_c vs. PBG; (b) the curve of ω_c vs. $\delta\omega/\omega_i$.

4. CONCLUSIONS

In summary, the dispersion properties of 3D FPPCs and MFPPCs with woodpile lattices are theoretically studied, respectively. For the case of 3D MFPPCs, only the magneto-optical Voigt effect is considered, and the PBG properties of the extraordinary mode are investigated. The calculated results demonstrate that for the presented 3D FPPCs, larger PBG can be achieved than the 3D dielectric-air PCs, 3D function dielectric PCs and 3D plasma-dielectric PCs with the same lattices. For the proposed 3D MFPPCs, the narrower PBG for the extraordinary mode can be obtained compared with the 3D function dielectric PCs and 3D PPCs with the same lattices. The computed results also show that the bandwidths and locations of those PBGs can be adjusted by altering the parameters. For those two cases, the red shifts can be seen in the edges of PBGs, when the values of the function coefficients of function dielectric and R are enhanced. On the contrary, the blue shifts can be found in the edges of PBGs when ω_p increases. Larger PBG can be gotten with a larger function coefficient of function dielectric or R . A larger ω_p will lead to a narrow PBG for both cases, and larger PBGs appear in the low- ω_p . However, for 3D FMPPCs, larger PBG can be gotten in the low- ω_c region. The computed results also show us an approach to realize the reconfigurable devices based on the proposed FPPCs and FMPPCs.

ACKNOWLEDGMENT

This work was supported by the Open Research Program in China's State Key Laboratory of Millimeter Waves (Grant No. K201927).

REFERENCES

1. Yablonovitch, E., "Inhibited spontaneous emission in solid-state physics and electronics," *Phys. Rev. Lett.*, Vol. 58, 2059, 1987.
2. John, S., "Strong localization of photons in certain disordered dielectric super-lattices," *Phys. Rev. Lett.*, Vol. 58, 2486, 1987.
3. Joannopoulos, J. J., R. D. Meade, and J. N. Winn, *Photonic Crystals: Molding the Flow of Light*, Princeton University Press, New Jersey, 1995.
4. Hojo, H. and A. Mase, "Dispersion relation of electromagnetic wave in one-dimensional plasma photonic crystals," *J. Plasma Fusion Res.*, Vol. 80, 89, 2004.

5. Ginzburg, V. L., *The Propagation of Electromagnetic Waves in Plasmas*, Pergamon, Oxford, New York, 1970.
6. Zhang, H. F., S. B. Liu, X. K. Kong, L. Zou, C. Z. Li, and W. S. Qing, "Enhancement of omnidirectional photonic band gaps in one-dimensional dielectric plasma photonic crystals with a matching layer," *Phys. Plasmas*, Vol. 19, 022103, 2012.
7. Li, C., S. Liu, X. Kong, H. Zhang, B. Bian, and X. Zhang, "A novel comb-like plasma photonic crystal filter in the presence of evanescent wave," *IEEE Trans. Plasma Sci.*, Vol. 39, 1969–1973, 2011.
8. Zhang, H. F. and S. B. Liu, "Magneto-optical faraday effects in dispersive properties and unusual surface plasmon modes in the three-dimensional magnetized plasma photonic crystals," *IEEE Photonics J.*, Vol. 6, 5300112, 2014.
9. Guo, B., "Photonic band gap structures of obliquely incident electromagnetic wave propagation in a one-dimension absorptive plasma photonic crystal," *Phys. Plasmas*, Vol. 16, 042508, 2009.
10. Qi, L., "Photonic band structures of two-dimensional magnetized plasma photonic crystals," *J. Appl. Phys.*, Vol. 111, 073301, 2012.
11. Zhang, H. F., "Investigations on the two-dimensional aperiodic plasma photonic crystals with fractal Fibonacci sequence," *AIP Adv.*, Vol. 7, 2059–549, 2017.
12. Shiveshwari, L., "Zero permittivity band characteristics in one-dimensional plasma dielectric photonic crystal," *Optik*, Vol. 122, 1523, 2011.
13. Dehnavi, Z. N., H. R. Askari, M. Malekshahi, and D. Dorranean, "Investigation of tunable omnidirectional band gap in 1D magnetized full plasma photonic crystals," *Phys. Plasmas*, Vol. 24, 093517, 2017.
14. Qi, L., Z. Yang, and T. Fu, "Defect modes in one-dimensional magnetized plasma photonic crystals with a dielectric defect layer," *Phys. Plasmas*, Vol. 19, 012509, 2012.
15. Sakai, O. and K. Tachibana, "Plasmas as metamaterials: A review," *Plasma Sources Sci. Technol.*, Vol. 21, 013001, 2012.
16. Zhang, H. F., S. B. Liu, and Y. C. Jiang, "The properties of photonic band gap and surface plasmon modes in the three-dimensional magnetized photonic crystals as the mixed polarized modes considered," *Journal of Plasma Physics*, Vol. 81, 905810201, 2015.
17. Ardakani, A. G., "Nonreciprocal electromagnetic wave propagation in one-dimensional ternary magnetized plasma photonic crystals," *J. Opt. Soc. Am. B*, Vol. 31, 332, 2014.
18. Mehdian, Z. Mohammadzahery, and A. Hasanbeigi, "The effect of magnetic field on bistability in 1D photonic crystal doped by magnetized plasma and coupled nonlinear defects," *Phys. Plasmas*, Vol. 21, 012101, 2014.
19. Zhang, H. F., S. B. Liu, J. P. Zhen, and Y. J. Tang, "The right circular polarized waves in the three-dimensional anisotropic dispersive photonic crystals consisting of the magnetized plasma and uniaxial material as the Faraday effects considered," *Phys. Plasmas*, Vol. 21, No. 3, 032127, 2014.
20. Zhang, H. F. and S. B. Liu, "The properties of surface plasmon modes and switching gap for extraordinary mode in the three-dimensional magnetized plasma photonic crystals based on the Vogit effects," *IEEE Journal of Quantum Electronics*, Vol. 50, No. 7, 518–588, 2014.
21. Zhang, H. F., S. B. Liu, H. Yang, and X. K. Kong, "Analysis of photonic band gap in dispersive properties of tunable three-dimensional photonic crystals doped by magnetized plasma," *Phys. Plasmas*, Vol. 20, 032118, 2013.
22. Qi, L. and X. Zhang, "Band gap characteristics of plasma with periodically varying external magnetic field," *Solid State Commun.*, Vol. 151, 1838, 2011.
23. Zhang, H. F., S. B. Liu, X. K. Kong, B. R. Bian, and Y. N. Cuo, "Dispersion properties of two-dimensional plasma photonic crystals with periodically external magnetic field," *Solid State Commun.*, Vol. 152, 1221, 2012.
24. Zhang, H. F., S. Liu, and X.-K. Kong, "Properties of anisotropic photonic band gaps in three-dimensional plasma photonic crystals containing the uniaxial material with different lattices," *Progress In Electromagnetics Research*, Vol. 141, 267–289, 2013.

25. Zhang, H. F., S. B. Liu, and X. K. Kong, "dispersion properties of three-dimensional plasma photonic crystals in diamond lattice arrangement," *J. Lightwave Technol.*, Vol. 31, 1694, 2013.
26. Zhang, H. F., S. B. Liu, X. K. Kong, and R. B. Bian, "The characteristics of photonic band gaps for three-dimensional unmagnetized dielectric plasma photonic crystals with simple-cubic lattice," *Opt. Commun.*, Vol. 288, 82–90, 2013.
27. Ho, K. M., C. T. Chan, C. M. Soukoulis, R. Biswas, and M. Sigalas, "Photonic band gaps in three dimensions: New layer-by-layer periodic structures," *Solid State Commun.*, Vol. 89, 413–416, 1994.
28. Kopperschmidt, P., "Tetragonal photonic woodpile structures," *Appl. Phys. B*, Vol. 76, 729–734, 2003.
29. Fan, S. H., P. R. Villeneuve, and J. D. Joannopoulos, "Theoretical investigation of fabrication-related disorder on the properties of photonic crystals," *J. Appl. Phys.*, Vol. 78, 1415–1418, 1995.
30. Zhang, H. F., S. B. Liu, and X. K. Kong, "Investigation of anisotropic photonic band gaps in three-dimensional magnetized plasma photonic crystals containing the uniaxial material," *Phys. Plasmas*, Vol. 20, 092105, 2013.
31. Zhang, H. F., S. B. Liu, and Y. C. Jiang, "Tunable all-angle negative refraction and photonic band gaps in two-dimensional plasma photonic crystals with square-like Archimedean lattices," *Phys. Plasmas*, Vol. 21, 092104, 2014.
32. Maksymov, I. S., L. F. Marsal, M. A. Ustyantsev, and J. Pallarès, "Band structure calculation in two-dimensional Kerr-nonlinear photonic crystals," *Opt. Commun.*, Vol. 248, 469–477, 2005.
33. Azuma, H., "Quantum computation with Kerr-nonlinear photonic crystals," *Journal of Physics D: Applied Physics*, Vol. 41, 369–374, 2012.
34. Youssefi, B., M. K. Moravvej-Farshi, and N. Granpayeh, "Two bit all-optical analog-to-digital converter based on nonlinear Kerr effect in 2D photonic crystals," *Opt. Commun.*, Vol. 285, 3228–3233, 2012.
35. Zhang H. F., "Three-dimensional function photonic crystals," *Physica B*, Vol. 525, 104–113, 2017.
36. Liu, X. J., Y. Liang, J. Ma, S. Q. Zhang, H. Li, X. Y. Wu, and Y. H. Wu, "Two-dimensional function photonic crystals," *Physica E*, Vol. 85, 227–237, 2017.
37. Wu, X. Y., S. Q. Zhang, B. J. Zhang, X. J. Liu, J. Wang, H. Li, N. Ba, X. G. Yin, and J. W. Li, "The effect of defect layer on transmissivity and light field distribution in general function photonic crystals," *Physica E*, Vol. 53, 1, 2013.
38. Fan, S., P. R. Villeneuve, and J. D. Joannopoulos, "Large omnidirectional band gaps in metallodielectric photonic crystals," *Phys. Rev. B*, Vol. 54, 11245–11251, 1996.
39. McIntosh, K. A., L. J. Mahoney, K. M. Molvar, O. B. McMahon, S. Verghese, M. Rothschild, and E. R. Brown, "Three-dimensional metallodielectric photonic crystals exhibiting resonant infrared stop bands," *Appl. Phys. Lett.*, Vol. 70, 2937, 1997.
40. Li, J., G. Sun, and C. T. Chan, "Optical properties of photonic crystals composed of metal-coated spheres," *Phys. Rev. B*, Vol. 73, 075117, 2006.
41. Feng, L., M. H. Lu, V. Lomakin, and Y. Fainman, "Plasmonic photonic crystals with complete bandgap for surface plasmon polariton waves," *Appl. Phys. Lett.*, Vol. 93, 231105, 2008.
42. Tserkezis, C., "Effective parameters for periodic photonic structures of resonant elements," *J. Phys. Condens Matter*, Vol. 21, 155404, 2009.
43. Tserkezis, C., N. Stefanou, G. Gantzounis, and N. Papanikolaou, "Understanding artificial optical magnetism of periodic metal-dielectric-metal layered structures," *Phys. Rev. B*, Vol. 84, 115455, 2011.
44. Park, D. J., C. Zhang, J. C. Ku, Y. Zhou, G. C. Schatz, and C. A. Mirkin, "Plasmonic photonic crystals realized through DNA-programmable assembly," *Proc. Ntnl. Acad. Sci.*, Vol. 112, 977, 2015.
45. Dobson, D. C., J. Gopalakrishnan, and J. E. Pasciak, "An efficient method for band structure calculations in 3D photonic crystals," *Journal of Computational Physics*, Vol. 161, 668–679, 2000.

46. Zhang, H. F., G. W. Ding, H. M. Li, and S. B. Liu, "Complete photonic band gaps and tunable self-collimation in the two-dimensional plasma photonic crystals with a new structure," *Phys. Plasmas*, Vol. 22, 022105, 2015.
47. Ho, K. M., C. T. Chan, and C. M. Soukoulis, "Existence of a photonic gap in periodic dielectric structures," *Phys. Rev. Lett.*, Vol. 65, 3152, 1990.
48. Li, L., "Use of Fourier series in the analysis of discontinuous periodic structures," *J. Opt. Soc. Am. A*, Vol. 13, 1870, 1996.